Bollettino di Geofisica Teorica ed Applicata Vol. 58, n. 1, pp. 1-15; March 2017
DOI 10.4430/bgta0187

Brittle-ductile analogue modelling of piedmont arcs: the influence of pushing-from-behind in gravity-driven models

A. Jiménez-Bonilla[1], A. Crespo-Blanc[2], J.C. Balanyá[1], I. Expósito[1] and M. Díaz-Azpiroz[1]

[1] *Departamento de Sistemas Físicos, Químicos y Naturales, Universidad de Pablo de Olavide, Sevilla, Spain*

[2] *Departamento de Geodinámica - IACT, Universidad de Granada - CSIC, Granada, Spain*

(Received: November 14, 2016; accepted: April 8, 2017)

ABSTRACT We performed analogue experiments to investigate the genesis and the progressive formation of piedmonts. A silicone-sand parallelepiped was bounded by wood strips. The central part of the front strip was removed to permit the analogue material to flow through a gate, by gravity only in the first experiment, and also pushed from behind in the second one. In both cases, a piedmont arc formed in front of the gate, whose end points represented the arc tips of natural piedmonts. Deformation in the brittle layer (sand) was mostly accommodated by normal faults in the first experiment, versus oblique-slip faults in the second experiment. Extension separated blocks that rotated in opposite directions. In the piedmont, arc-parallel and arc-perpendicular stretching was observed. Our results can be applied to toe thrust belts or collapsed foreland fold-and-thrust belts, floored by evaporites and/or overpressured shale formations.

Key words: analogue model, piedmont arc, normal fault, arc-perpendicular and arc-parallel stretching, block rotation.

1. Introduction

A salient is an arcuate component of a curved fold-and-thrust belt, convex towards the foreland [see review in Marshak (2004)]. It is a purely descriptive term based on the geometric elements which characterize it (Macedo and Marshack, 1999). In order to classify such structures in terms of the mechanism of curvature formation, various authors highlight: a) the geometry of the displacement field and the strain trajectory path (Hindle and Burkhard, 1999), and/or b) the angular relationship between the structural trend and secondary imposed curvatures through vertical-axis rotations (Weil and Sussman, 2004). Following these criteria, three end-member types of curved fold-and-thrust belt are distinguished: 1) oroclines, formed by pure bending of an initially straight belt; 2) primary arcs, formed during uniform displacement direction; 3) progressive arcs, whose curvature is acquired progressively during the orogenic formation through strongly divergent displacement directions. Within progressive arcs, piedmonts are a particular case characterized by divergent transport direction, resulting in foreland-ward increasing arc-parallel extension ["spreading" arc: Hindle and Burkhard (1999)].

Among the wide range of approaches for the understanding of the genesis of curved fold-and-thrust belts, analogue modelling permits researchers to investigate the progressive deformation of arcs at different scales (Keep, 2000; Lickorish *et al*., 2002; Crespo-Blanc and González-Sánchez, 2005; Pastor-Galán *et al*., 2012; Toscani *et al*., 2014). In particular, piedmont arcs were modelled through the horizontal spreading of viscous analogue material through a free boundary, either to model the spreading of a continental lithosphere with layers of honey, silicone, and sand (Gautier *et al*., 1999) or to model spreading nappes in ductile conditions only with silicone (Gilbert and Merle, 1987; Merle, 1989).

No analogue experiments were conducted to simulate the formation of a piedmont arc at upper crustal conditions, which are those at which fold-and-thrust belts develop. In this paper, we present the results of brittle-viscous (sand-silicone) experiments, which simulate the formation of piedmont arcs in front of a gate through which the analogue material spreads out. In natural cases, the two sides of the gate represent the arc end points of natural piedmonts floored by a weak layer (evaporitic formations or water-saturated shales). The wooden strip which bound the gate represents basement obstacles [e.g., Brasilia foreland fold-and-thrust belt: Reis and Alkmim (2015)], areas without weak rocks and/or with high thickness variation of the sedimentary rocks forming the fold-and-thrust belt [e.g., Zagros fold-and-thrust belt: Navabpour *et al*. (2014)] or any structure which impedes the horizontal flow of the weak rocks lying below the sedimentary rocks [e.g., the delta flanks and shale pinch-out in the Niger Delta: Corredor *et al*. (2005)].

Our experimental approach permits: a) a study of the progressive deformation that takes place during the development of the piedmont arc and of the resulting highly partitioned deformation mode in the upper brittle layer, and b) a comparison of our results with those obtained either in purely ductile or lithospheric analogue models. Finally, a comparison with natural cases of foreland and toe fold-and-thrust belts will be presented (Niger Delta and Sulaiman Arc).

2. Model set-up, material properties, and scaling

A simplified sketch of the experimental apparatus and model setting can be seen in Fig. 1. The brittle behaviour of the sedimentary rocks characteristic of fold-and-thrust belts is simulated by quartz sand (grain size between 0.2 and 0.3 mm; internal friction coefficient Φ=37º), while silicone putty reproduces the ductile flow of shales saturated in water and evaporites (transparent Rhodosil Gum FB of Rhone-Poulenc). Table 1 shows the characteristic values of the length, density, viscosity, and velocity (this latter only for the second group of experiments) for both natural case (*n* subscript) and analogue materials (*m* subscript), by assuming a length ratio (L_n/L_m) of $5x10^4$ (2 cm in the experiment represents 1 km in nature). We calculated the different parameters of Table 1 according to the following equations.

For brittle materials (Merle, 2015):

$$[\tau_{0m} = (\tau_{0n}) / (\varrho^* g^* l^*)] \quad (1)$$

where τ_0 is the cohesion; ϱ^*, g^*, l^* are the scaling factors between the model and the natural cases of the density of the brittle layer, the gravity, and the length, respectively. Cohesion in

dry sand for normal stress less than 250 Pa is zero, and using a 1.5-cm thick layer of sand, the normal stress is 260 Pa at its base, assuming the density of the dry sand shown in Table 1. Using the minimum τ_{0n} for weak rocks (Davis and Engelder, 1985), 5 MPa, the calculated cohesion τ_{0m} is 74 Pa, and thus the cohesion of the dry sand used in our experiments is quite low to reproduce the natural cases. However, this lower cohesion does not significantly change the experimental results.

For ductile materials, according to the approach of Weijemars and Schmeling (1986) where:

$$\eta_m = \eta_n \{(v_n/v_m) / [(\varrho_n g_n l^2_n)/(\varrho_m g_m l^2_m)]\} \quad (2)$$

the viscosity for the analogue material using a range of viscosities of shales and evaporites in nature from 10^{17} to 10^{21} Pa·s (Table 1) is between 10^3 and 10^8 Pa·s. Hence, the silicone putty used in our experiments ($5 \cdot 10^4$ Pa·s) would be appropriate.

The pre-deformational package, 33 cm long and 42.5 cm wide, was made up of a 2-cm thick silicone layer overlaid by a 1.5-cm thick layer of sand (Fig. 1). This silicone/sand ratio of 1.33 is the maximum ratio of weak rocks/post-extensional sequences observed in the fold-and-thrust belts with which we will compare our results, that is, ratios from 0.8 to 1.5 in the Niger Delta (Corredor *et al*., 2005) and ca. 1 in the Sulaiman Arc (Humayon *et al*., 1991). A grid with a scale of 3 cm placed on top of the initial parallelepiped was used as a passive marker. A Mylar sheet floored the sandbox, and sand was used to confine the lateral portions of the parallelepiped, while its frontal part was bounded by a wooden strip divided into three parts (Fig. 1). The central part (20 cm long, Rf in Fig. 1) was removed at the beginning of the experiments; whereas the other two were fixed (Ff in Fig. 1). This permitted the free flow of the material that constituted the initial parallelepiped out of this gate in the frontal part of the experiment. In the first experiment, the sand/silicone package only flowed by gravity. In order to observe the influence of convergence in the same direction as the symmetry axis of the piedmont (Fig. 1), we carried out a second group of experiments, in which the package was pushed from behind by a rigid backstop at the rear of the model (wood piece B in Fig. 1) during the whole experiment. In this case, the velocity used for the second experiments was 0.82 cm/hour, at which the silicone behaves like a viscous material (Luján *et al*., 2006).

Both types of experiments were stopped when approximately half of the piedmont area was occupied by silicone (240 minutes in Experiment 1; 330 minutes in Experiment 2 with

Table 1 - Scaling parameters between nature and the model. Legend: a = Bonini (2001); b = Weijermars *et al*. (1993); c = Cotton and Koyi (2000); d = Mukherjee *et al*., (2010); e = Davis and Engelder (1985).

Parameters	Symbol	Unit	Nature (N)	Model (M)	Scaling factor (N/M)
Length	L	m	1×10^3	2×10^{-2}	5×10^4 (length ratio)
Density (sand)	δsan	kg/m3	2400 (a)	1770	1.35
Density (silicone)	δsil	kg/m3	2200 (b, c)	980	2.24
Viscosity	η	Pa s	From 10^{17} to 10^{21} (d)	0.5×10^5	2×10^8 to 2×10^{13}
Convergence velocity (only for Experiment 2)	Vc	m/s	3.1×10^{-10} (a) to 7.2×10^{-10} (1.0-2.3 cm/y) (b)	2.27×10^{-6} (0.82 cm / h)	1.36×10^{-4}
Cohesion (sand)	τ	Pa	5×10^6 (e)	-	1×10^5

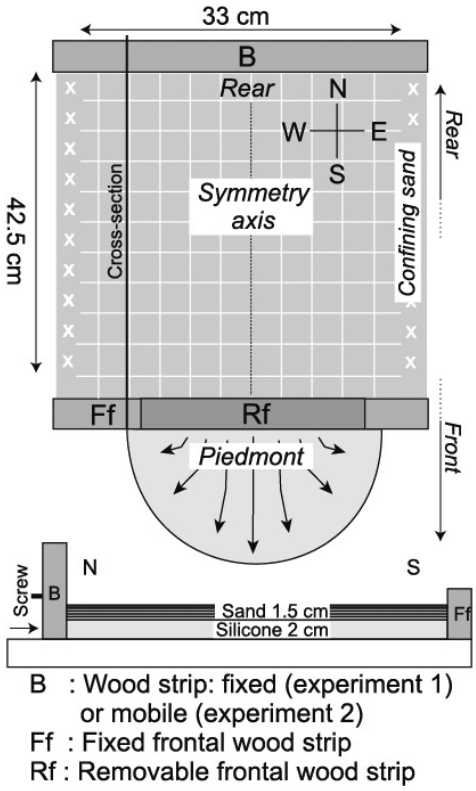

Fig. 1 - Simplified sketch of the experimental apparatus and model setting in plan view and cross-section.

a backstop movement of 4.75 cm). The progressive deformation was recorded by time lapse photography in zenithal view, and oblique photographs were taken at the end of the experiments. To check the consistency of the results, the experiments were repeated. The most representative ones are shown below. The experiments were carried out in the Analogue Modelling Laboratory located in Granada (Geodynamics Department, Andalusian Earth Science Institute).

3. Results

Fig. 1 shows the terms used in the description of the experiment results. The progressive deformation of both experiments is illustrated with photographs together with line drawings in which the chronology of the structures' nucleation is indicated with numbering (Figs. 2, 3, and 4 and videos of the experiments available in Supplementary Materials). In Fig. 3, the line drawings were made at the beginning (after 60 minutes) and the end of the experiments. Additionally, an intermediate stage chosen after the development of characteristic structures was represented for both experiments (after 150 and 120 minutes in experiments 1 and 2, respectively). Particle paths have been drawn from successive photographs of zenithal views (Fig. 5).

In both types of models, the silicone overlaid by sand flowed from the inner domain through the gate from the very beginning of the experiment. A piedmont structure formed, in which arc-parallel lengthening accompanied by opposite-direction rotations took place as shown by the grid on top of the parallelepiped and the corresponding particle displacement (Figs. 2 to 5).

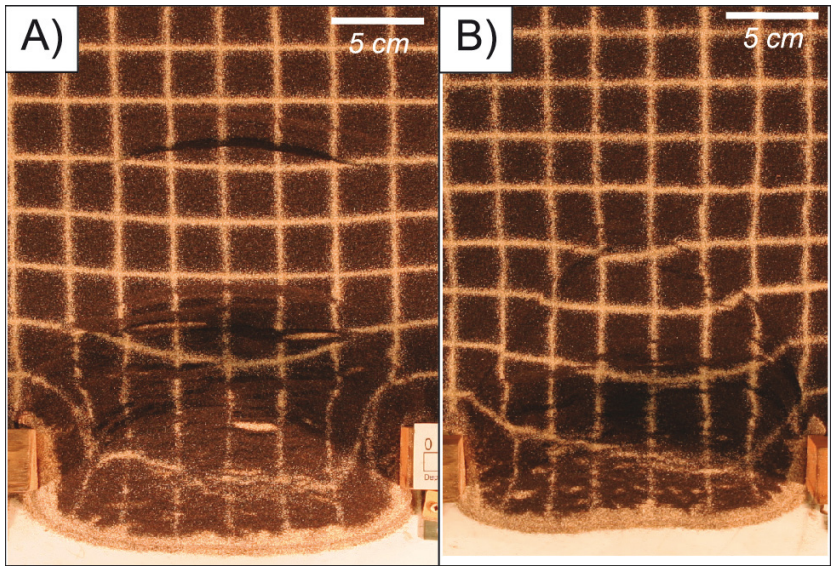

Fig. 2 - Photographs of the very early stages (t 30 min) of Experiment 1 (A) and Experiment 2 (B). Grid: 3 cm.

The vertical axis rotations in the piedmont were as expected (e.g., Hindle and Burkhard, 1999): clockwise to the left of the piedmont symmetry axis as positioned in Fig. 3 and anticlockwise to the right. In the most frontal part of the piedmont, the upper sand levels were driven to the bottom of the deformed parallelepiped producing a frontal recumbent fold [rolling zone *sensu* Merle (1989); Video 1 in Supplementary Materials].

The transfer of material produced extension, subparallel to the flow direction in both the inner domain and the piedmont, accommodated by normal, oblique, and strike-slip fault systems (Fig. 3). These fault systems favoured the ascent of silicone that separated blocks capped by sand, which rotated differentially during progressive deformation and in which discrete structures were recognized. These latter are described according to each type of experiment.

3.1. Experiment 1: gravity-driven model

The first structures to form were millimetric-spaced, dipping to the front (i.e., southwards), normal faults situated in the most frontal part of the inner domain (Fig. 2A). They formed straight around the gate (faults 1 and 2 in Fig. 3A) and concave with respect to the sense of movement in the inner part of the model (Fault 3 in t^1 of Fig. 3A). Extension quickly propagated to the rear of the parallelepiped (i.e., northwards) and a conjugated asymmetric, normal fault system developed inwards, forming a slightly concave graben with the master fault dipping towards the front of the model (Fig. 2A; Fault System 4 in Fig. 3A). The system was situated 17 cm from the gate, that is approximately the gate width, and bounded the deformed part of the inner domain. During progressive deformation, the faults grew laterally while a left-lateral strike-slip fault, located at the right part of the model, linked the rear fault system with the structures developed at the frontal part of the sandpack (Fault 5 in Fig. 3A). This strike-slip fault accommodated differential displacement between blocks A and B, and hence acted as a tear fault.

With ongoing flow of the material through the gate, the piedmont grew and extension proceeded in the rear part. The rear normal fault system grew laterally, drawing a mirror arc with

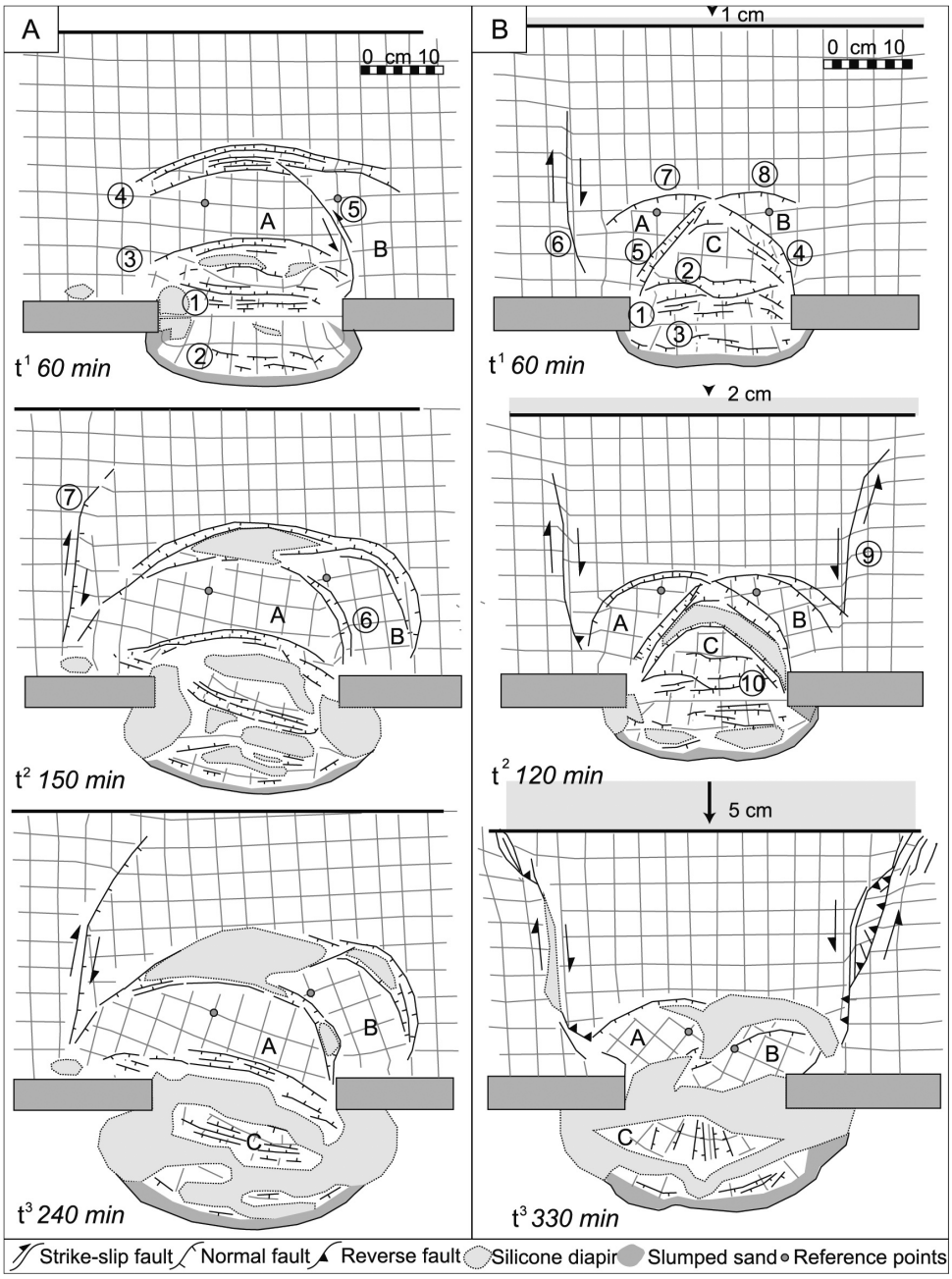

Fig. 3 - Line drawings of Experiment 1 (A) and Experiment 2 (B) at different stages. Numbering indicates the nucleation sequence of the faults.

respect to the piedmont, although wider (see t^2 in Fig. 3A). Enhanced by its buoyancy, silicone reached the surface in both the piedmont and the inner domain normal faults. Tear Fault 5 became oblique, acquiring a dominant normal dip-slip component, as shown by the grid markers and particle displacement (Figs. 3A and 5, respectively). At the same time, another oblique normal fault developed close and subparallel to the first one (Fault 6 in Figs. 3A and 5A),

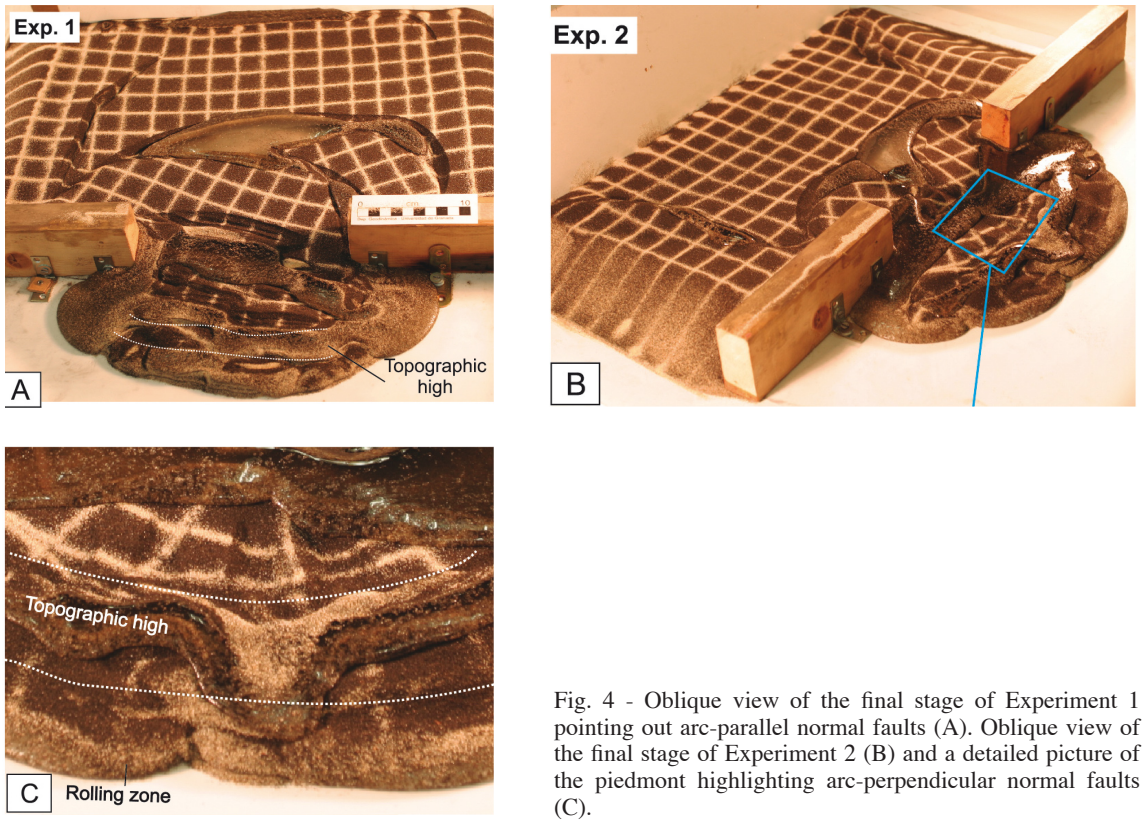

Fig. 4 - Oblique view of the final stage of Experiment 1 pointing out arc-parallel normal faults (A). Oblique view of the final stage of Experiment 2 (B) and a detailed picture of the piedmont highlighting arc-perpendicular normal faults (C).

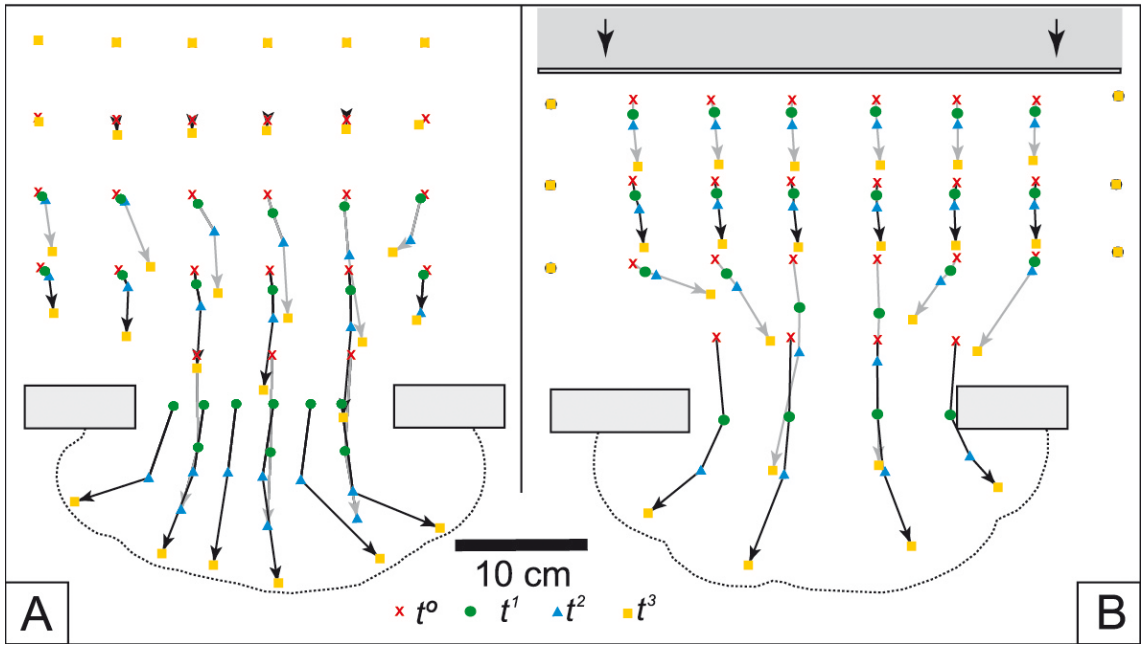

Fig. 5 - Pattern of particle displacement distinguishing four stages for Experiment 1 (A) and Experiment 2 (B). We show the passive markers that may be followed during the deformation or that are useful to delve into the kinematics.

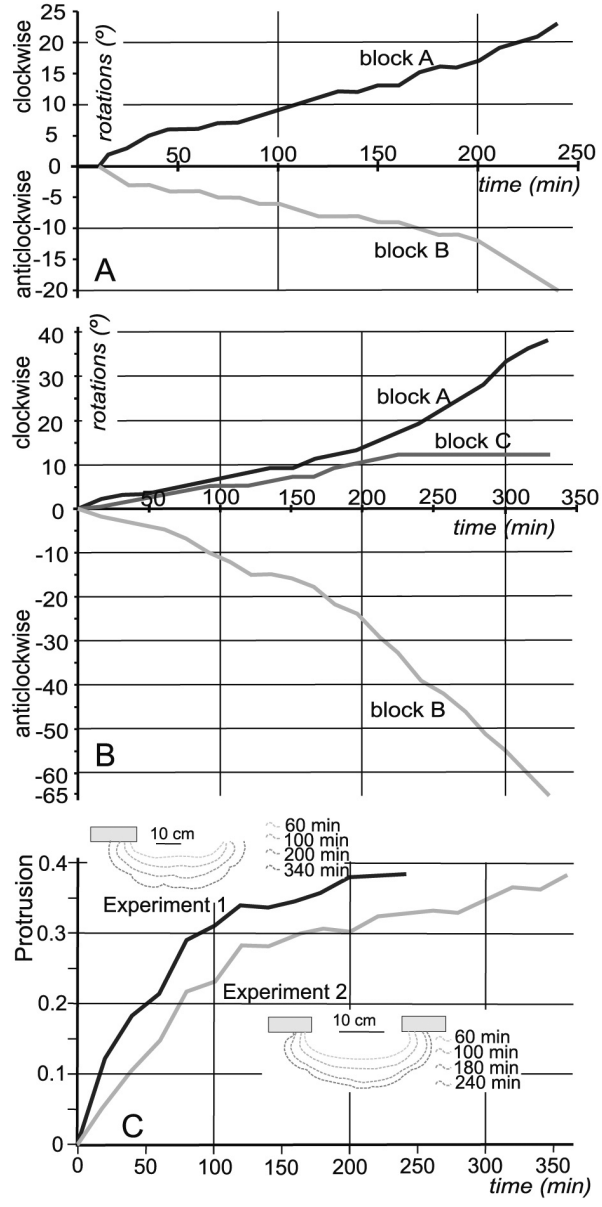

Fig. 6 - Graphs showing block rotations in Experiment 1 (A) and Experiment 2 (B) during the time and the variation of protrusion together with the piedmont outline during progression of deformation (C).

defining a narrow graben, and a normal-dextral fault developed to the left of the model (Fault 7 in Figs. 3A and 5A). The array of faults within the inner domain produced the individualization of two blocks, which suffered vertical axis rotations during progressive deformation. The amount of rotation and velocity were estimated by measuring the grid marker orientation over time and are illustrated in Fig. 6A. Block A rotated clockwise, while Block B rotated anticlockwise. At the completion of the experiment, a third block was isolated by silicone in the piedmont (Block C in t^3 of Fig. 3A). Block C together with Block A rotated 23º clockwise, while Block B rotated 20º anticlockwise (Fig. 6A).

The estimated bulk extension along the symmetry axis of the model, from its rear (fixed wood strip, Fig. 1) to the apical part of the piedmont was around 156%. The silicone invaded

most of the piedmont zone (Figs. 3A and 4A), where arc-parallel extension was evidenced by both the grid pattern and the lengthening of its outer boundary (53 cm long vs. 20 cm of gate width, that is, a 265% extension). No normal faults striking perpendicular to the arc were detected within the brittle layer of Block C (Fig. 4A). Thus, arc-parallel stretching must have been accommodated by deformation in the silicone which surrounded this block. The protrusion grade of the piedmont outer boundary can be estimated in the sense of Macedo and Marshak (1999), that is, the ratio between the amplitude and the cord line length. Its evolution during time is shown in Fig. 6C.

3.2. Experiment 2: gravity-driven and pushed-from-behind model

At the onset of the experiment, normal faults with a millimetric spacing formed, with a similar geometry to those above the piedmont of Experiment 1 (Fig. 2B and t^1 of Fig. 3B, Faults 1 to 3). When the experiment proceeded, the volume change due to the outward flow of the silicone associated with the piedmont formation was partly compensated in the rear part by the backstop movement. Extension propagated backwards into the inner domain, triggering the nucleation of two conjugated and symmetrical normal fault systems, at approximately 45º in relation to the backstop movement (fault systems 4 and 5; Fig. 2B and t^1 of Fig. 3B). Together with Fault System 2, they formed a triangle that bounded Block C. At the intersection zone of these fault systems, two other symmetrical frontal-dipping normal faults formed (faults 7 and 8 in Fig. 3B). They were concave with respect to the backstop movement. When deformation proceeded, faults 7 and 8 lengthened towards the lateral parts of the model, isolating two other blocks (A and B; t^2 of Fig. 3B). Additionally, a dextral strike-slip fault zone nucleated at the left side of the model (Fault 6; t^1 of Fig. 3B). At this stage, it constituted a transtensional fault zone,

Fig. 7 - Detailed photographs of the strike-slip fault zones developed at both laterals of Experiment 2.

given that the block on the left side remained roughly immobile while the one on the right side moved towards the gate (see grid in Fig. 3B and particle displacement in Fig. 5B).

With progressive deformation, the development of normal faults favoured the ascent of silicone (t^2 of Fig. 3B). As the orientation of these normal faults was oblique with respect to the symmetry axis, their movement also showed a strike-slip component which produced the progressive clockwise and anticlockwise vertical-axis rotation of blocks A and B, respectively (fault systems 7 and 8). They rotated up to 38º and 65º, respectively, while in the centre of the model, Block C did not rotate considerably (Figs. 3B and 6B). In the right part of the model, a sinistral strike-slip fault zone nucleated (Fault 9), conjugated in respect to Fault 6. Fault 9 had a subordinated reverse dip-slip component in its central segment, thus forming a transpressive fault zone (Figs. 3B and 5B). Both fault zones, slightly oblique with respect to the convergence direction (5º to 15º), played the role of transfer faults. In the piedmont, the silicone pierced its front while a normal fault developed in its rear part (Fault 10 in Fig. 3B).

Because of the orientation variations along strike of the strike-slip Fault Zone 9 with respect to the backstop, a restraining bend developed associated with subordinated thrust, which produced the uplift of its central part (Figs. 3B and 7). By contrast, in the strike-slip Fault Zone 6, the left block remained roughly immobile, while the right one moved towards the gate, as shown by the opening of the N-S grid from one part to the other of the strike-slip fault (Fig. 7) and the convergent pattern of the particle displacement field (Fig. 5B), thus causing the silicone outcrop.

It is worth noting that, even though the backstop pushed from behind the deformed parallelepiped, neither folds nor thrusts developed in the inner domain. The undeformed grid on the sand showed that most of the rear part of the model acted as a pushed-from-behind rigid body (Fig. 3B), limited by the backstop and bounded by: a) the normal faults situated in the rear part of the inner domain (faults 7 and 8, Fig. 3B), and b) the strike-slip fault zones (faults 6 and 9). The estimated bulk extension along the symmetry axis of the model was around 119%, lower than the 156% of Experiment 1.

Within the piedmont, arc-perpendicular normal faults developed (Figs. 3B, 4B, and 4C). They remained preserved on the surface of Block C, and produced an extension of 120% and 160% in the northern and southern markers, respectively. Nevertheless, at the outer boundary, the piedmont showed an extension of 230% (final length of 46 cm vs. 20 cm of gate width). The arc-parallel stretching must have been mainly accommodated by deformation in the silicone, which occupied a great part of the piedmont (Figs. 3B, 4B, and 4C).

4. Discussion

4.1. Comparison between experiments 1 and 2

In both experiments, the deformation in the brittle layer (sand) was accommodated by discrete normal, strike-slip, and oblique faults, with a variable orientation and movement from one type of experiment to the other. Indeed, these faults showed a dominant normal component in the gravity-driven model (Experiment 1) and dominant oblique and strike-slip in the gravity-driven and pushed-from-behind model (Experiment 2). In the inner domains of both experiments, these fault systems individualized blocks which rotated differentially. It is also

remarkable that the presence of discrete normal faults in sand producing arc-parallel extension was limited to the model of Experiment 2. The fact that the analogue material of the inner part was forced to go through the gate produced a convergent pattern of the particle displacement field in both experiments, although it was more pronounced in the pushed-from-behind model (Experiment 2; Fig. 5). In the latter, the analogue material first moved straight in a N-S direction, channeled by the strike-slip fault zones, and then changed its flow direction abruptly, converging towards the gate (see arrows in Fig. 8B). Hence, the induced E-W shortening in the inner domain when the material was approaching the gate was solved by the opposite rotation of blocks A and B (Fig. 3B), as no folds have been recorded (see the evolution of the distance points marked on Fig. 3).

Within the piedmont, arc-perpendicular normal faults developed in Experiment 2, while they were not observed in Experiment 1 (Figs. 3B, 4B, and 4C). Additionally, a lower protrusion grade of the piedmont was observed in Experiment 2 with respect to Experiment 1. Finally, even with a backstop actuated in the rear of Experiment 2, neither folds nor thrusts developed in the inner domain. By contrast, in both experiments, the large N-S extension favoured the development of isolated blocks capped by sand and separated by silicone walls. Both experiments may represent the first stages of raft tectonics, even if such tectonics need more than 200% of stretching (Duval *et al.*, 1992; Guglielmo *et al.*, 1997) and lower values were reached in both experiments.

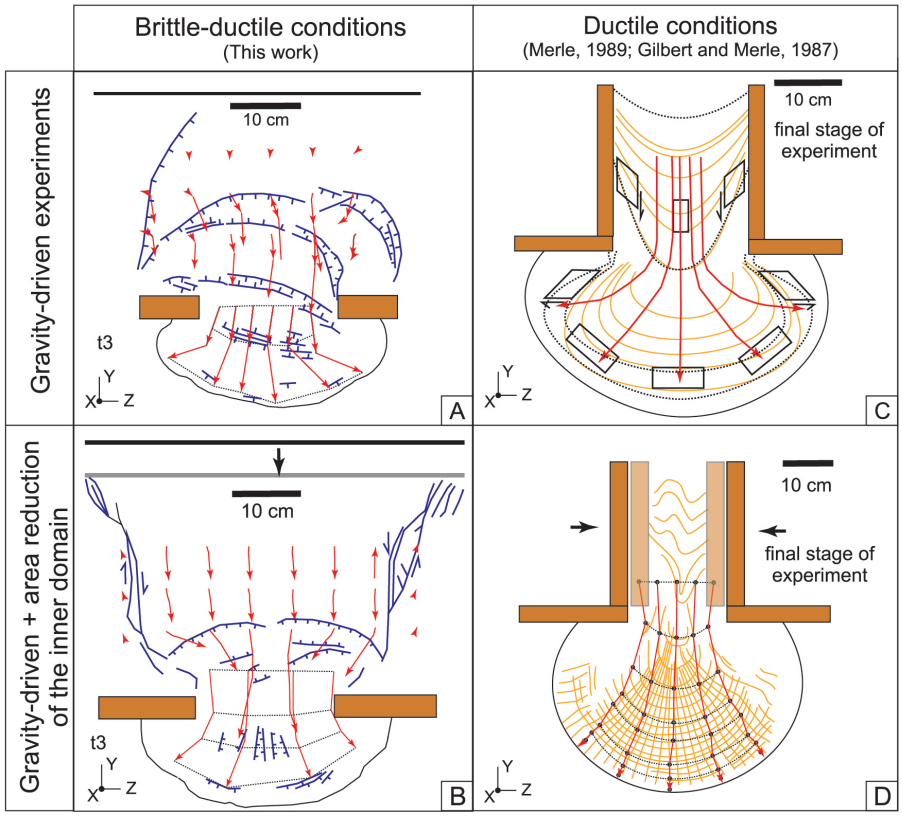

Fig. 8 - Diagram comparing ductile models, using silicone, and our brittle-ductile, sand-silicone models.

4.2. Comparison of our results with previous analogue models

The experiments performed by Merle (1986, 1989) and Gilbert and Merle (1987) generated piedmont arcs, although in their models only silicone was used as analogue material and the inner part consisted of a channel (opened at the beginning of the experiment), instead of a rectangle bounded by a gate. Moreover, this channel was eventually squeezed, which reduced the area of the inner domain during the experiment. Their results are summarized and compared with ours in Fig. 8. The gravity-driven experiments of these authors display homogeneous deformation and the particle displacement in the inner domain is parallel to the channel walls. The difference in particle velocity within the channel is accommodated by ductile shear zones parallel and close to the channel walls (Fig. 8C). When the channel is squeezed, the particle displacement pattern shows shortening across the channel and the silicone is affected by folds (Fig. 8D). This contrasts with the rigid-block rotations which characterized the inner domain in our brittle-ductile experiments. Moreover, in our experiments, the development of piedmonts in brittle-ductile conditions is accommodated by discrete, regularly spaced normal faults in the sand layer, which produced both arc-parallel and arc-perpendicular extension. The protrusion in our models is lower than in the silicone experiments. Finally, in both silicone and sand-silicone models, a more divergent pattern of particle displacement can be observed in gravity-driven models (Figs. 8A and 8C vs. 8B and 8D).

We have no information along vertical sections of our models concerning the deformation of the silicone. Nevertheless, the asymmetric development of the normal faults systems in the sand layer (e.g., Fault Zone 4 of Experiment 1; Fig. 3A) suggests simple shear in the uppermost levels of the silicone, with southward transport of the hanging wall (towards the gate). If correct, this would imply that the presence of a detached rigid body on top of the viscous layer could have modified the vertical distribution of the silicone strain pattern in comparison with silicone models, where pure shear dominates the upper levels of silicone [see the mechanical model governed by viscous spreading in Fig. 8 (Merle, 1986)]. The existence of a mechanical discontinuity between sand layer and silicone might induce a simple shear-dominated deformation in the silicone levels lying just below the sand.

Hatzfeld *et al*. (1997) and Gautier *et al*. (1999) modelled the horizontal spreading of a continental lithosphere towards a free boundary leading to the formation of a piedmont arc with honey, silicone, and sand models. Similar to our experiments, the transfer of material towards the piedmont is balanced by normal to oblique faults within the inner domain. Nevertheless, as these authors chose to model lithospheric scale processes, the thickness of the brittle layer with respect to the silicone is relatively small (3 to 4 times smaller). Consequently, the deformation is much more distributed than in our models, and no silicone wall pierces the brittle layer.

4.3. Applicability of brittle-ductile models to shallow-crustal natural cases

A natural analogue of Experiment 1 may be toe fold-and-thrust belts floored by evaporites and/or shales saturated in water. Indeed, their deformation is achieved exclusively by gravity and they do not require additional shortening (Worrall and Snelson, 1989; Cobbold *et al*., 1995). Within a toe fold-and-thrust belt, three zones are differentiated downslope (e.g., Connors *et al*., 2009; Krueger and Grant, 2011; Mahanjane and Franke, 2014; Wu *et al*., 2015):

1) a zone of extension characterized by the growth of normal faults whose traces are generally concave with respect to the flow direction, and in which weak rocks (silicone)

can be present (raft tectonics). In our model this zone is simulated by the inner domain, characterized by the extension that balances the transfer of material from the inner zone to the piedmont (Figs. 2A and 3A). Overall, the normal faults of the inner domain draw a mirror arc with respect to the arc (Figs. 2A and 3A) outlined by the toe fold-and-thrust belt (Wu *et al.*, 2015). In natural cases comparable to our model, passive rotation of structures and block rotation have been described with similar features to those observed during our model evolution [Okari oil field in the Niger Delta: e.g., Aminu and Olorunniwo (2011); Figs. 2A, 3A, and 6A];

2) a zone characterized by radial outward transport direction and strong raft tectonics, akin to the piedmont of our experiment (Figs. 3A and 4A). In this zone, both arc-perpendicular and arc-parallel extension have been detected in toe fold-and-thrust belts (Wu *et al.*, 2015);
3) a zone where the extension in the first two zones is balanced with shortening, which generates a fold-and-thrust belt. In our model, these compressive structures correspond to the curved topographic high (Fig. 4A).

At plan view, the curvature of some toe fold-and-thrust is considered to be a primary feature (Wu *et al*., 2015) and, therefore, spreading would have played a limited role in its progressive curved shape. In the Niger Delta case, however, the existence of two clearly differentiated lobes of higher curvature in the outer part seems to be related to the interference between the toe fold-and-thrust belt and basement obstacles in the topography of the underlying oceanic crust [the Charcot and Chain fracture zones: Wu *et al*. (2015)]. Even though the degree of blocking is different, the gate sides of our model would have played a comparable role.

In Experiment 2, shortening generated by the backstop movement did not compensate for the extension produced by gravitational spreading, and fold-and-thrust belts are not developed. Nevertheless, the transport of material from the inner domain towards the piedmont is governed by two nearly parallel strike-slip fault zones (faults 6 and 9 of Fig. 3B; Fig. 7). In natural cases, similar arrays of structures are observed in the Sulaiman Arc. The pattern of this arc has been modelled and interpreted by Copley (2012) as the result of gravitational spreading of a mountain range, composed of viscous rocks, onto a rigid footwall, crystalline rock domains. Macedo and Marshack (1999) proposed that the thickness variation of a pre-deformational basin whose depocentre was located at the apex of the arc mainly controlled the progressively curved shape of the Sulaiman Arc. These two models of curvature formations are not exclusive. In this sense, it is noteworthy that our experiments induce the formation of an obstacle-controlled curve (the piedmont) due to the disposal of the fixed sides of the gate. In natural fold-and-thrust arcuate belts, these obstacles are commonly basement highs, similar to the basin sides of the Sulaiman Arc.

5. Conclusions

We simulated the progressive deformation in piedmont arcs with analogue models that include a parallelepiped made up of silicone overlaid by sand, and a gate through which the material can flow freely. We conducted two types of experiments: a) gravity-driven and b) gravity-driven and push-from-behind models.

In both types of experiments, the transfer of material towards the piedmont was achieved in the inner domain by transfer faults together with normal fault systems that propagated towards the rear of the model. Both types of faults developed in the sand layer. Extension favoured the development of isolated blocks capped by sand separated by silicone walls, similar to the first stages of raft tectonics.

In the inner domain, the converging displacement pattern behind the gate produced shortening, which was accommodated by the opposite-direction rotation of blocks. Outwards from the gate, the development of the piedmonts resulted in a divergent particle displacement which generated both arc-parallel and arc-perpendicular extension.

The deformation accommodated by discrete structures in the sand layer situated over the silicone contrasts with the homogeneous deformation described in previously published experiments of piedmont arcs made up of only silicone.

The deformation mode observed in our models can be applied to natural cases. The gravity-driven experiment is similar to toe thrust-belts such as the Okari oil field in the Niger Delta, while our gravity-driven and push-from-behind experiment developed some features observed in convergent fold-and-thrust belts, such as the Sulaiman Arc, whose arcuate shape has been explained as gravitational spreading triggered by a topographic gradient.

Acknowledgements. This study was supported by projects RNM-0451, CGL2013-46368-P, and EST1/00231. We also thank the revision from O. Merle and an anonymous referee.

REFERENCES

Aminu M.B. and Olorunniwo M.A.; 2011: *Reservoir characterization and paleo-stratigraphic imaging over the Okari Field, Niger Delta, using neural networks*. Leading Edge, **30**, 650-655.

Bonini M.; 2001: *Passive roof thrusting and forelandward fold propagation in scaled brittle-ductile physical models of thrust wedges*. J. Geophys. Res., **106**, 2291-2311.

Cobbold P.R., Szatmari P., Demercian L.S., Coelho D. and Rossello E.A.; 1995: *Seismic and experimental evidence for thin-skinned horizontal shortening by convergent radial gliding on evaporites, deep-water Santos Basin, Brazil*. Am. Assoc. Pet. Geol. Mem., **65**, 305-321.

Connors C.D., Radovich B., Danforth A. and Venkatraman S.; 2009: *The structure of the offshore Niger Delta*. Trabajos de Geología, **29**, 182-188.

Copley A.; 2012: *The formation of mountain range curvature by gravitational spreading*. Earth Planet. Sci. Lett., **351-352**, 208-214.

Corredor F., Shaw J.H. and Bilotti F.; 2005: *Structural styles in the deep-water fold and thrust belts of the Niger Delta*. AAPG Bull., **89**, 753-780.

Cotton J. and Koyi H.; 2000: *Modeling of thrust front above ductile and frictional detachments: application to structures in the Salt Range and Potwar Plateau, Pakistan*. Geol. Soc. Am. Bull., **112**, 351-363.

Crespo-Blanc A. and González-Sánchez A.; 2005: *Influence of indenter geometry on arcuate fold-and-thrust wedge: preliminary results of analogue modelling*. Geogaceta, **37**, 11-14.

Davis D.M. and Engelder T.; 1985: *The role of salt in fold-and-thrust belts*. Tectonophys., **119**, 67-88.

Duval B., Cramez C. and Jackson M.P.A.; 1992: *Raft tectonics in the Kwanza Basin, Angola*. Mar. Pet. Geol., **9**, 389-404.

Gautier P., Brun J.P., Moriceau R., Sokoutis D., Martinod J. and Jolivet L.; 1999: *Timing, kinematics and cause of Aegean extension: a scenario based on a comparison with simple analogue experiments*. Tectonophys., **315**, 31-72.

Gilbert E. and Merle O.; 1987: *Extrusion and radial spreading beyond a closing channel*. J. Struct. Geol., **9**, 481-490.

Guglielmo G. Jr., Schultz-Ela D.D. and Jackson M.P.A.; 1997: *Raft tectonics in the Kwanza Basin, Angola: an animation*. A BEG hypertext multimedia publication on the Internet: <www.beg.utexas.edu/indassoc/agl/animations/AGL96-MM-003/index.html>.

Hatzfeld D., Martinod J., Bastet G. and Gautier P.; 1997: *An analog experiment for the Aegean to describe the contribution of gravitational potential energy*. J. Geophys. Res., **102**, 649-659.

Hindle D. and Burkhard M.; 1999: *Strain, displacement and rotation associated with the formation of curvature in fold belts: the example of the Jura Arc*. J. Struct. Geol., **21**, 1089-1101.

Humayon M., Lillie R.J. and Lawrence R.D.; 1991: *Structural interpretation of the eastern Sulaiman Foldbelt and Foredeep, Pakistan*. Tectonics, **10**, 299-324.

Keep M.; 2000: *Models of lithospheric-scale deformation during plate collision: effects of indentor shape and lithospheric thickness*. Tectonophys., **326**, 203-216.

Krueger S.W. and Grant N.T.; 2011: *The growth history of toe thrusts of the Niger Delta and the role of pore pressure*. AAPG Mem., **94**, 357-390.

Lickorish W.H., Ford M., Bürgisser J. and Cobbold P.R.; 2002: *Arcuate thrust systems in sandbox experiments: a comparison to the external arcs of the Western Alps*. Geol. Soc. Am. Bull., **114**, 1089-1107.

Luján M., Storti F., Rossetti F. and Crespo-Blanc A.; 2006: *Extrusion vs. accretion at the frictional-viscous décollement transition in experimental thrust wedges: the role of convergence velocity*. Terra Nova, **18**, 241-247.

Macedo J. and Marshak S.; 1999: *Controls on the geometry of foldthrust belt salients*. Geol. Soc. Am. Bull., **111**, 1808-1822.

Mahanjane E. and Franke S.D.; 2014: *The Rovuma Delta deep-water fold-and-thrust belts, offshore Mozambique*. Tectonophys., **614**, 91-99, doi:10.1016/j.tecto.2013.12.017.

Marshak S.; 2004: *Salients, recesses, arcs, oroclines, and syntaxes - A review of ideas concerning the formation of map-view curves in fold-thrust belts*. AAPG Mem., **82**, 131-156.

Merle O.; 1986: *Patterns of stretch trajectories and strain rates within spreading-gliding nappes*. Tectonophys., **124**, 211-222.

Merle O.; 1989: *Strain models within spreading nappes*. Tectonophys., **165**, 57-71.

Merle O.; 2015: *The scaling of experiments on volcanic systems*. Front. Earth Sci., **3**, 1-15, doi:10.3389/feart.2015.00026.

Mukherjee S., Talbot C.J. and Koyi H.A.; 2010: *Viscosity estimates of salt in the Hormuz and Namakdan salt diapirs, Persian Gulf*. Geol. Mag., **147**, 497-507.

Navabpour P., Barrier E. and McQuillan H.; 2014: *Oblique oceanic opening and passive margin irregularity, as inherited in the Zagros fold-and-thrust belt*. Terra Nova, **26**, 208-215.

Pastor-Galán D., Gutiérrez-Alonso G., Zulauf G. and Zanella F.; 2012: *Analogue modeling of lithospheric-scale orocline buckling: constraints on the evolution of the Iberian-Armorican Arc*. Geol. Soc. Am. Bull., **124**, 1293-1309, doi:10.1130/B30640.1.

Reis H. and Alkmim F.; 2015: *Anatomy of a basin-controlled foreland fold-thrust belt curve: the Três Marias salient, Sao Francisco Basin, Brazil*. Mar. Pet. Geol., **66**, 711-731, doi:10.1016/j.marpetgeo.2015.07.013.

Toscani G., Bonini L., Ahmad M.I., Di Bucci D., Di Giulio A., Galuppo C. and Seno S.; 2014: *Opposite verging chains sharing the same foreland: kinematics and interactions through analogue models (central Po Plain, Italy)*. Tectonophys., **633**, 268-282, doi:10.1016/j.tecto.2014.07.019.

Weijermars R. and Schmeling H.; 1986: *Scaling of Newtonian and non-Newtonian fluid dynamics without inertia for quantitative modelling of rock flow due to gravity (including the concept of rheological similarity)*. Phys. Earth Planet. Inter., **43**, 316-330.

Weijermars R., Jackson M.P.A. and Vendeville B.; 1993: *Rheological and tectonic modeling of salt provinces*. Tectonophys., **217**, 143-174.

Weil A.B. and Sussman A.J.; 2004: *Classifying curved orogens based on timing relationships between structural development and vertical-axis rotations*. Geol. Soc. Am., **383**, 1-15, doi:10.1130/0-8137-2383-3(2004)383[1:CCOBOT]2.0.CO;2

Worrall D.M. and Snelson S.; 1989: *Evolution of the northern Gulf of Mexico, with emphasis on Cenozoic growth faulting and the role of salt*. In: Bally A.W. and Palmer A.R. (eds), The Geology of North America: an Overview, Geol. Soc. Am., vol. A, pp. 97-138.

Wu J.E., McClay K. and Frankowicz E.; 2015: *Niger Delta gravity-driven deformation above the relict Chain and Charcot oceanic fractures zones. Gulf of Guinea: insights from analogue models*. Mar. Pet. Geol., **65**, 43-62.

Corresponding author: Alejandro Jiménez-Bonilla
Departamento de Sistemas Físicos, Químicos y Naturales, Universidad de Pablo de Olavide
Utrera Road km 1, 41013, Sevilla, Spain
Phone: +34 671 235154; e-mail: ajimbon@upo.es
Supplementary materials: two videos of the experiments are available at www3.inogs.it/bgta.